ELSEVIER

International Journal of Heat and Fluid Flow 22 (2001) 525–536

International Journal of HEAT AND FLUID FLOW

www.elsevier.com/locate/ijhff

Numerical evaluation of alternate tube configurations for particle deposition rate reduction in heat exchanger tube bundles

D. Bouris [a], G. Papadakis [b], G. Bergeles [a,*]

[a] *Laboratory of Aerodynamics, Department of Mechanical Engineering, National Technical University of Athens, 5 Heroon Polytechniou Avenue, 15710 Zografos, Athens, Greece*

[b] *Department of Mechanical Engineering, King's College London, Strand WC2R, 2LS, UK*

Received 13 September 2000; accepted 8 February 2001

Abstract

The potential of two passive techniques, namely elliptic-shaped tubes and asymmetric tube bundle arrangement, for deposition rate reduction in lignite-fired utility boiler heat exchangers is numerically studied through comparison with an in-line tube arrangement with circular tubes. The simulation is based on a two-dimensional calculation of the turbulent two-phase flow in heat exchanger tube bundles using a subgrid-scale model for the small-scale turbulent structures and a particle adhesion model for the particle–surface interaction. Large-scale motion is found to be an important mechanism for tube surface fouling. Of the three tube bundle arrangements that were studied, the in-line tube bundle with elliptic-shaped tubes shows the lowest fouling rates and pressure drop. Taking advantage of these, heat transfer rates might be increased by placing more rows in the same area.

Keywords: Tube bundles; Heat exchangers; Numerical simulation; Vortex shedding; Fouling

1. Introduction

All coals have a significant content of ash-forming inorganic material, which cannot be economically removed before combustion. This material forms deposits on the surfaces in and around the boiler, interfering with operation, causing unplanned shutdowns and reducing output and efficiency.

The possible savings that could be made by better control of ash deposition in coal-fired boilers in the US have been estimated at 400 million US$/yr (Couch, 1994) based on 1% increase in the heat transfer rate and 1% improvement in availability. Considering US coal-fired capacity to represent about one-third of the world total, the possible world-wide savings from reductions in costs due to slagging and fouling would be in the region 1000–1500 million US$/yr. These figures justify the considerable research and development effort that has been assumed in recent years to improve the understanding of ash deposition on the boiler surfaces. The ultimate objective is to minimize heat exchanger fouling while heat transfer augmentation is achieved.

In this context, the present paper is concerned with the efficiency, in terms of fouling behavior, of two proposals for passive fouling reduction methods: non-circular tubes and asymmetric tube bundle arrangement. The logic behind the proposed methods is that an elliptic-shaped tube will have a smaller frontal area and reduced vortex shedding so that fewer particles will deposit due to inertial impaction. The asymmetric tube bundle has been noted as having heat transfer rates somewhere between in-line and staggered arrangements (Wung et al., 1986) so that a displacement from the in-line arrangement could be expected to increase heat transfer while keeping fouling rates closer to the in-line arrangement than the staggered one.

The basic case is taken to be the in-line tube bundle with circular tubes. The numerical approach that is used is capable of simulating both the transitional and the unsteady character of the flow in the tube bundles. Thus, the effect of turbulence and large-scale structures on particle deposition is easily accounted for. An interesting discussion is presented in Rollet-Miet et al. (1999) regarding the numerical simulation of turbulent flow in tube bundles. Based on the results of previously held workshops on this type of flow, they conclude that Reynolds averaged Navier–Stokes (RANS) equation models do not provide sufficient accuracy. Although the predictions of the mean properties of the flow might be acceptable, the stress profile predictions are poor, even with Reynolds stress models. They go on to present a large eddy simulation (LES) of turbulent flow through a staggered tube bundle. According to Rollet-Miet et al. (1999), the superiority of the LES predictions is attributed to the fact that LES is better suited to flows where

* Corresponding author. Tel.: +301-772-1056; fax: +301-772-1057.
E-mail addresses: deme@fluid.mech.ntua.gr (D. Bouris), george.papadakis@kcl.ac.uk (G. Papadakis), bergeles@fluid.mech.ntua.gr (G. Bergeles).

0142-727X/01/$ - see front matter
PII: S0142-727X(01)00110-2

Notation

a, b	elliptic-shaped tube axes (m)
C_D	aerodynamic resistance coefficient
C_s	coefficient of Smagorinsky subgrid-scale model
D	diameter of base case tube (m)
d_p	particle diameter (m)
g	acceleration of gravity (m s^{-2})
k	thermal conductivity of fluid (W/m s)
K_{th}	thermophoresis coefficient (kg m^2 s^{-2})
l_ξ, l_η	metric coefficients for orthogonal curvilinear grid
m_p	particle mass (kg)
Nu	Nusselt number ($=q''_w D/k(T_{wall}-T_{flow})$)
Pr	Prandtl number ($=C_p\mu/k$)
q''_w	heat flux on wall (W/m^2)
Q_i, Q_P, Q'_A	impact energy, plastic deformation energy, adhesion energy (kg m^2 s^{-2})
Q_L, Q_{lift}	elastic wave propagation energy, lift force energy (kg m^2 s^{-2})
Re_{dg}	Reynolds number ($=U_{gap}D\rho/\mu$)
S_L, S_T	longitudinal and lateral spacing of tube centers in a tube bundle (m)
Stk	particle Stokes number ($=\rho_p d_p^2 U_b/18\mu D$)
S_0	transverse displacement of tube center in asymmetric arrangement (m)
$S_{\xi\xi}, S_{\eta\eta}, S_{\xi\eta}$	rate of strain (S_{ij}) components (s^{-1})
S_Φ	source terms for Navier–Stokes equations
T	temperature (K or °C)
t	time (s)
T_{SGS}	time scale of subgrid-scale motion (s)
u, U_b, U_{gap}	axial velocity, free stream bulk velocity, bundle gap velocity (m s^{-1})
v, V_r	lateral velocity, particle rebound velocity (m s^{-1})
$\vec{v}_g, \vec{v}_p$	gas velocity and particle velocity vector (m s^{-1})
x, y	Cartesian directions
y^+	non-dimensional distance from wall

Greeks

Γ	diffusion coefficients (kg m^{-1} s^{-1})
Δ	filter width of volume average (m)
μ_{eff}, μ, μ_t	effective, fluid and turbulent dynamic viscosity (kg m^{-1} s^{-1})
ξ, η	orthogonal curvilinear coordinate directions
ρ, ρ_p	fluid and particle density (kg m^{-3})
τ	particle relaxation time (s)

the size of the eddies (integral length scale of the turbulence) is comparable to that of the obstacles in the flow. Another feature that makes it difficult for RANS approaches to correctly simulate this type of flow is the fact that most tube bundle heat exchangers used in industry operate under subcritical conditions and have transitional regimes. LES is better suited to calculate these flow regions.

The approach presented here resembles large eddy simulation, although computations are performed in two dimensions only. This is dictated by the excessive amount of computing time and storage required to perform a three-dimensional large eddy simulation; several million cells would be required. Barsamian and Hassan (1997) have presented two-dimensional large eddy simulations of turbulent cross-flow in tube bundles. They argue that, for this type of flow, a two-dimensional LES can be considered almost as reliable as a three-dimensional one with the exception of specific properties such as the pressure distribution after boundary layer separation and the reverse cascade phenomenon in turbulence energy transfer. With these limitations in mind, as well as the fact that turbulence is inherently three dimensional, we prefer to call the approach used here a two-dimensional simulation using a subgrid-scale model rather than a large eddy simulation. By omitting the third dimension, computer storage economy is achieved and the separating boundary layers can be resolved using very fine mesh. Bouris and Bergeles (1999) found that, for the purpose of the type of study performed here, correct representation of the mean properties, the statistical turbulence quantities and the major unsteady characteristics will be the most influential in particle deposition.

In order to assess the code validity, numerical results are compared against measurements taken in a laboratory-scale model of the standard in-line tube arrangement used by the Public Power Corporation (PPC) of Greece. The flow in the full-scale tube bundles is then calculated at industrial operating conditions and a parametric study is performed regarding tube bundle arrangement and tube shape. This is, to the best of the authors' knowledge, the first numerical study presented in the literature of the effect of the large-scale motion on heat exchanger fouling. Bouris and Bergeles (1996) performed calculations of deposition rate in tube bundles but for a steady-state calculation of the flow. Wang and Squires (1996) simulated particle deposition in a vertical channel flow using LES and examined the effect of the SGS fluctuations on the particle deposition behavior but they were mainly concerned with the turbulent velocity fluctuations. The effect of the vortex shedding in a tube bundle is, as will be shown in this paper, an important mechanism in particle deposition in tube bundles that should not be overlooked.

The paper is organized as follows: the numerical methodology is briefly discussed and the numerical results are compared against experimental measurements so as to assess the reliability of the method. Three tube bundles – an in-line tube bundle with circular tubes, an in-line tube bundle with tubes of elliptic cross-section and an asymmetrically staggered tube bundle with circular tubes – are then compared in terms of particulate deposition rate for each tube row and particle diameter, as well as pressure drop and heat transfer rates.

2. Numerical methodology

The numerical simulation of the subcritical flow in tube bundles is a difficult task since transitional effects as well as vortex shedding are dominant characteristics of the flow field. In the present paper a time-dependent simulation using a subgrid-scale model is performed in two dimensions for the subcritical flow through three different tube bundles.

The procedure used is similar to that of Bouris and Bergeles (1999). The numerical method is based on the solution of the volume averaged Navier–Stokes equations (according to Schumann, 1975) on an orthogonal curvilinear grid. The resulting equations have the following general conservative form:

$$\frac{\partial}{\partial t}(\rho\Phi)+\frac{1}{l_\xi l_\eta}\frac{\partial}{\partial\xi}(\rho u_\xi l_\eta\Phi)+\frac{1}{l_\xi l_\eta}\frac{\partial}{\partial\eta}(\rho v_\eta l_\xi\Phi) - \frac{1}{l_\xi l_\eta}\frac{\partial}{\partial\xi}\left(\mu_{eff}\frac{l_\eta}{l_\xi}\frac{\partial\Phi}{\partial\xi}\right)-\frac{1}{l_\xi l_\eta}\frac{\partial}{\partial\eta}\left(\mu_{eff}\frac{l_\xi}{l_\eta}\frac{\partial\Phi}{\partial\eta}\right)=S_\Phi, \qquad (1)$$

where l_ξ and l_η are the spatially varying metric coefficients related to the orthogonal curvilinear coordinates (ξ,η) and S_Φ is the source term. For $\Phi = 1, u_\xi, v_\eta$, the continuity, and the momentum equations are obtained, respectively. It should be pointed out that velocities u_ξ, v_η are always defined as being normal to the grid lines of constant ξ,η, respectively. The source term involves rather large but well-known expressions in computational fluid dynamics and is not presented here due to lack of space but it can be found in Mouzakis and Bergeles (1991). The effective viscosity is given by the formula $\mu_{\text{eff}} = \mu + \mu_t$, where μ_t is calculated for the subgrid-scale fluctuations according to the model of Smagorinsky (1963) and Lilly (1967):

$$\mu_t = \rho(C_s\Delta)^2\left|\bar{S}\right| = \rho(C_s\Delta)^2(2\bar{S}_{i,j}\bar{S}_{i,j})^{1/2} \quad i,j = \xi,\eta, \tag{2}$$

where

$$\begin{aligned}
\overline{S}_{\xi\xi} &= 2\left(\frac{1}{l_\xi}\frac{\partial u}{\partial \xi} + \frac{v}{l_\xi l_\eta}\frac{\partial l_\xi}{\partial \eta}\right),\\
\overline{S}_{\eta\eta} &= 2\left(\frac{1}{l_\eta}\frac{\partial v}{\partial \eta} + \frac{u}{l_\xi l_\eta}\frac{\partial l_\eta}{\partial \xi}\right),\\
\overline{S}_{\xi\eta} &= \frac{1}{l_\xi}\frac{\partial v}{\partial \xi} + \frac{1}{l_\eta}\frac{\partial u}{\partial \eta} - \frac{v}{l_\xi l_\eta}\frac{\partial l_\eta}{\partial \xi} - \frac{u}{l_\xi l_\eta}\frac{\partial l_\xi}{\partial \eta}.
\end{aligned} \tag{3}$$

In Eq. (2) Δ is the filter width, defined as $\Delta = (\Delta\xi\Delta\eta)^{1/2}$ while the constant C_s is taken to be equal to 0.1. Velocities are stored at the center of the computational cells and the original SIMPLE algorithm (Patankar and Spalding, 1972) is used to deal with the pressure coupling of the momentum and continuity equations. In order to avoid the checkerboard pressure field, the method proposed by Rhie and Chow (1983) is employed.

A fully implicit method is used for the solution of the above equations i.e., the momentum, continuity and energy equations are converged at each time step prior to proceeding to the next one. For the computation of the temporal term, a first-order Euler discretization is employed. For the discretization of the convection terms (second and third term in the general transport Eq. (1)) a higher order bounded scheme developed by Papadakis and Bergeles (1995) is used. For the diffusion terms (fourth and fifth term in Eq. (1)) the central difference scheme is used. Periodic boundary conditions are used in the lateral direction when appropriate while the no-slip condition is applied at wall boundaries. The maximum observed y^+ value for the base case in-line arrangement ranged from 3 to 5, which puts the first grid point in the linear region of the boundary layer for most of the simulation. Rollet-Miet et al. (1999) reported mean values of y^+ in the range of 1.5–4 but the instantaneous peak values were much higher necessitating the use of wall functions. The two-dimensional simulation used here allows for sufficient grid density near the wall so wall functions are not required.

Regarding the particulate phase, one-way coupling is considered (i.e., the particles do not affect the flow field and turbulence) since the mass loading is only 1%. The particles are considered spherical, non-rotating and with a density much larger than that of the carrier gas so only the following forces are considered to affect particle motion: drag, gravity and thermophoresis (due to temperature gradients). Although thermophoresis is important only for micron and submicron particles while for larger particles the primary mechanism for adhesion is inertial impaction, the thermophoretic term was included in the equation of particle motion for completeness. The particle motion equation is

$$\begin{aligned}
\rho_p\frac{\pi d_p^3}{6}\frac{d\vec{v}_p}{dt} &= \frac{\pi}{6}d_p^3(\rho_p - \rho)\vec{g} - K_{th}\frac{\vec{\nabla}T}{T}\\
&\quad - C_D\pi\frac{d_p^2}{8}\rho\left(\vec{v}_p - \vec{v}_g\right)\left|\vec{v}_p - \vec{v}_g\right|,
\end{aligned} \tag{4}$$

where d_p is the particle diameter, v_p, v_g are the particle and carrier gas phase velocities, respectively, ρ_p, ρ are the particle and gas densities, respectively, T is the temperature, C_D is the non-linear drag coefficient (Clift et al., 1978), and finally K_{th} is the thermophoresis coefficient defined by Talbot et al. (1980).

Regarding the gas fluid velocity we assume that this is the one produced from the resolved field, i.e., the contribution of the subgrid scales on particle dispersion is neglected. It is expected that this assumption will affect mostly the smaller particles, which are more responsive to subgrid-scale motions occurring in smaller time scales. In order to justify this assumption one can compare the characteristic time scale of the subgrid-scale stresses to the particle relaxation time. The first time scale is defined in terms of the filter width (Δ) and the velocity scale ($\Delta|\bar{S}|$), i.e., $T_{SGS} = \Delta/(\Delta|\bar{S}|) = 1/|\bar{S}|$. The particle relaxation time (τ) is defined as the rate of response of particle acceleration to the relative velocity between the particle and the carrier fluid. The mathematical expression is $\tau = \rho_p d_p^2/18\mu$ where μ is the fluid viscosity. For the full-scale in-line calculation, the ratio T_{SGS}/τ was $\ll 1$ at all areas near the cylinders for the smallest particle diameter used (23 μm) while for the main flow passages in between the cylinders it was below 2. The effect of comparable T_{SGS} and τ on particle deposition in a vertical turbulence channel flow was investigated by Wang and Squires (1996). In their simulation the ratio T_{SGS}/τ was between 1 and 10, so they performed a second calculation incorporating the effects of the SGS fluctuations on the particle motion. Although T_{SGS} and τ were comparable, they found that the SGS velocity fluctuations did not have a large effect on the predicted deposition. If the diameter distributions were finer and smaller particles were present, then the SGS fluctuations would be more influential to the solid-phase calculation. Based on the previous findings and the facts that T_{SGS}/τ was $\ll 1$ close to the cylinders and that the particle motion in the areas between the cylinders is mostly affected by the large-scale vortices (as will be shown later) it was decided, at a first approximation, to neglect the effect of SGS fluctuations on the particle motion. Although this is a first approximation, the fact that, as *Re* is increased, SGS will carry an increasing fraction of turbulence kinetic energy (for fixed grid) and thus its effect will become more important, should be kept in mind.

The adhesion or rebound of the particles upon hitting the surface of a tube is determined by an energy balance at the point of impact. This takes into account the material properties of the particle and surface in order to calculate the elastic and plastic deformations while the surface energy is used to determine the forces holding the particle to the surface. Thus the particle rebound velocity is given by

$$V_r = \left[\frac{2}{m_p}\left(Q_i - Q_P - Q'_A - Q_L + Q_{lift}\right)\right]^{(1/2)}, \tag{5}$$

where m_p is the particle mass. The initial kinetic energy of the particle at impact (Q_i) is lost to plastic deformation energy (Q_P) (Wall et al., 1988) and dissipated as energy due to elastic wave propagation (Q_L) (Reed, 1985). The remaining energy (stored as elastic energy) is then returned to the particle and if it is larger than the energy due to attractive forces between particle and surface (Q'_A), then the particle will rebound, otherwise it will stick to the surface. If rebound occurs, then the normal rebound velocity is calculated. The attractive forces are mostly due to van der Waals–London dispersion forces (Fowkes, 1964). Other attractive forces, e.g., due to electro-

static effects, are not important for the particle size ranges in the applications being investigated. Q_{lift} is the aerodynamic lift energy that is gained by the particle due to hydrodynamic lift forces (Saffman, 1965). The tangential rebound velocity depends on the impact angle of the particle and is calculated according to Bitter (1963).

The expressions of these energy terms are quite complex and for a particle of known size and velocity they are functions of material properties of the particle and the surface to which it impacts: Young's modulus, Poisson's ratio, elastic yield limit of the softer of the two materials, particle density and interfacial surface energy derived from the dispersive surface energies of the two materials. Material properties were selected to correspond to fly ash material as sampled by the PPC of Greece from their lignite utility boilers (Bouris and Bergeles, 1996). The model can account for both clean tubes and fouled tubes through modification of the material properties of the surface. In fact, in the present computations, in areas where particles have already deposited, the surface properties become equal to the particle properties.

A much more detailed analysis and validation of the adhesion model against experimental measurements of particle deposition onto a single circular cylinder in high-temperature particle-laden cross-flow can be found in Bouris and Bergeles (1996). The agreement of the predicted variation of particle deposition rate with the angle (measured from the front stagnation point) against experiments was acceptable for a wide range of particle diameters. The same model is used here to examine the fouling behavior for three heat exchanger geometries.

3. Numerical studies of tube bundle arrangements

3.1. General description

Three tube bundle arrangements were examined using the in-line tube bundle with circular tubes as a base case. The actual dimensions and flow conditions of this arrangement were provided by the PPC of Greece. The superheater tube bundle consist of tubes, 38 mm in diameter (D), in an in-line arrangement with normalized transverse and longitudinal spacings S_T/D and S_L/D equal to 3.63 and 2.1, respectively. The gas flow velocities over the tube bundles are estimated to be equal to 9–10 m/s.

Two variants were examined with the purpose of identifying the effect of tube arrangement (asymmetrically placed tubes) and of tube shape (elliptic-shaped tubes) on the particle deposition characteristics. Based on studies appearing in the literature, the effects of tube shape and arrangement have indicated that they could have a positive influence on the heat transfer rates of the heat exchanger (Ota et al., 1984, 1986;

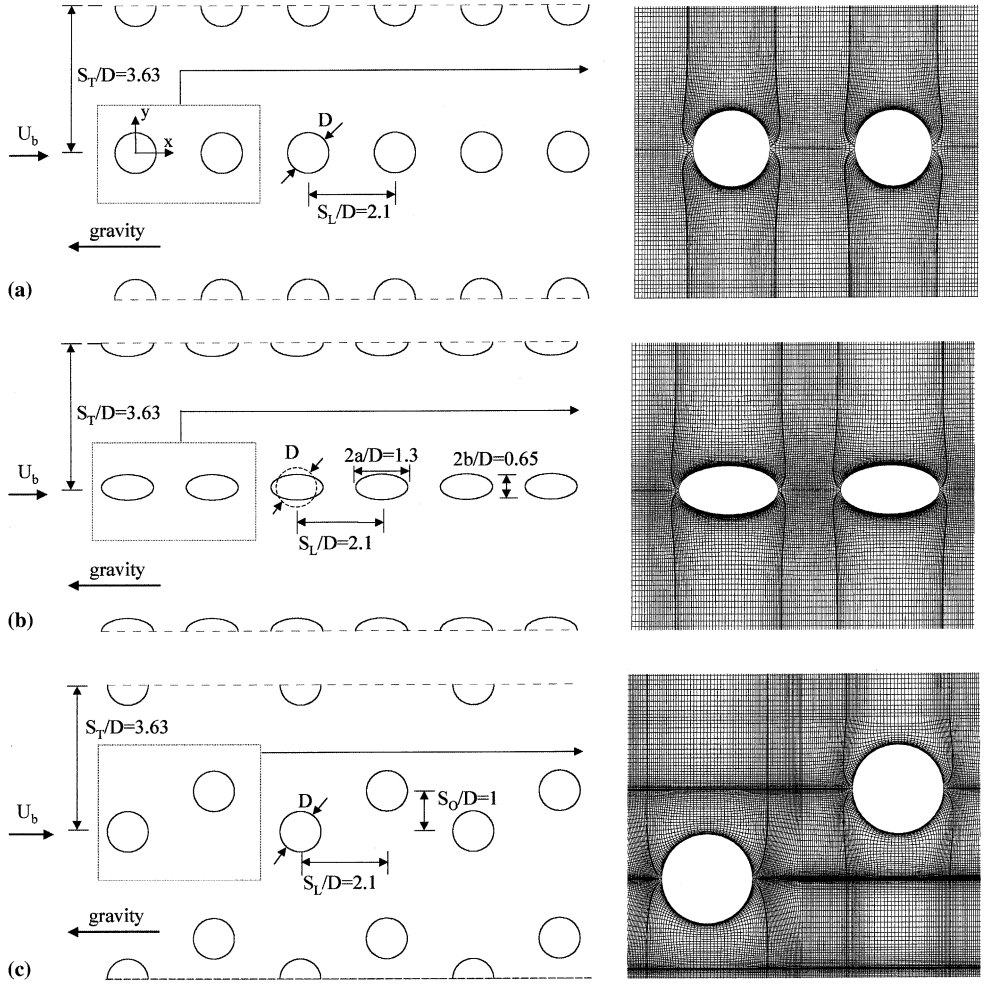

Fig. 1. Cross-section of the tube bundles examined and close-up view of the orthogonal curvilinear grid used: (a) in-line; (b) elliptic; (c) asymmetric tube bundle arrangements.

Wung et al., 1986). In this study, it was also expected that they might reduce fouling rates due to the smaller frontal area and streamlined shape of the elliptic tubes and the reduced vortex shedding intensity for both configurations. The asymmetric tube arrangement was constructed by shifting every other row of the in-line tube bundle by one diameter in the transverse direction. The elliptic-shaped tubes were designed with an axis ratio of 1:2 and in such a way that the heat transfer area is kept the same as that in the tube bundles with circular tubes. The normalized longitudinal and transverse ratios remain the same if the characteristic reference length is taken to be the equivalent circular tube diameter that provides the same circumferential area.

The three tube arrangements along with a close-up view of the associated computational grid of two cylinders are shown in Fig. 1.

3.2. Validation of the numerical methodology in the lab-scale tube bundle arrangement

In King's College London, tube bundle models were designed and constructed to simulate the flow in heat exchangers in lignite utility boilers in the power generation industry. The tube bundles of the industrial configurations were scaled down by a factor of 3.8 and detailed experimental measurements regarding the mean and rms velocities as well as the velocity spectra were obtained behind all rows. These are documented in Konstantinidis et al. (2000).

The experimental tube bundle arrangement is the same as in Fig. 1(a) where the coordinate system (x, y) is also indicated. All of the bundle's 1 tubes were included in the simulation using a computational mesh consisting of 91 405 cells (505×181). Part of the grid is shown in Fig. 1(a). A uniform velocity profile was used at the inlet (located $2.1D$ upstream of the first row). At the exit, zero normal derivatives were used for all quantities ($\partial\Phi/\partial x = 0, \Phi = u_\xi, v_\eta, p$). The $Re_{d,g}$ number (based on the gap velocity) was 3400. This number is very close to the Re number corresponding to the operating conditions of the heat exchangers in lignite utility boilers. The results are presented in non-dimensional form based on tube diameter (D) and the bulk velocity upstream of the bundle (U_b). The integration time step was 1.6×10^{-3} s and at least 2^{12} time steps were used for calculating mean quantities after fully developed flow conditions were reached. About 40–50 iterations per time step were needed for convergence.

Generally, good matching was found between the measurements and computations with deviations at the recirculation areas (Fig. 2). Although separation and reattachment of the flow on the tube surfaces is well predicted, in the recirculation zone at $(X/D = 5.1)$ there is an overprediction of the axial velocity.

The rms velocities were generally well predicted except in the areas between the flow lanes (between cylinder rows, $Y/D = 1.5$–2) where they were slightly underpredicted (Fig. 3). In order to monitor the frequency at which the vortices are shed from each cylinder, the velocity time series behind each cylinder in the central row were recorded. The calculated Strouhal number (based on the gap velocity) was found to be equal to 0.151 while the measured value is 0.141 (7.3% difference). Possible improvements to the methodology would be the incorporation of the inlet turbulent velocity fluctuations instead of using a steady inflow, the upgrading of the temporal discretization to second degree accuracy, and a more accurate discretization of the convection terms. However, for the purpose of the deposition studies to be performed, the general level of accuracy was considered to be acceptable. A similar level of agreement was observed for the other two arrangements as well (results are not presented for brevity of presentation).

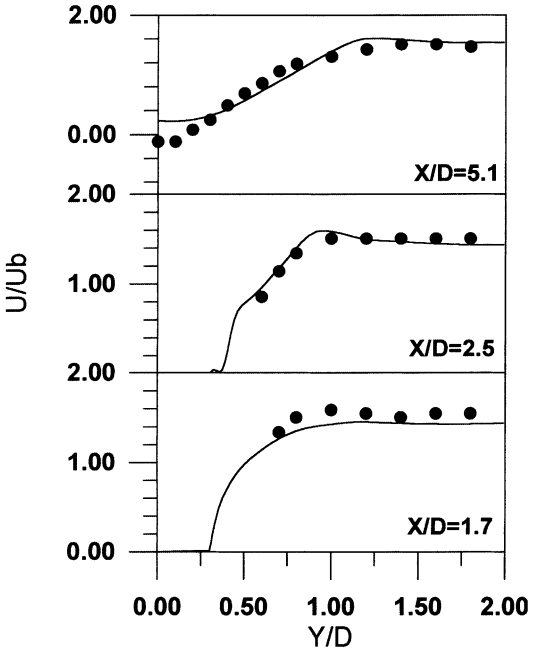

Fig. 2. Comparison between measurements (•) and predictions (lines) for time mean axial velocities.

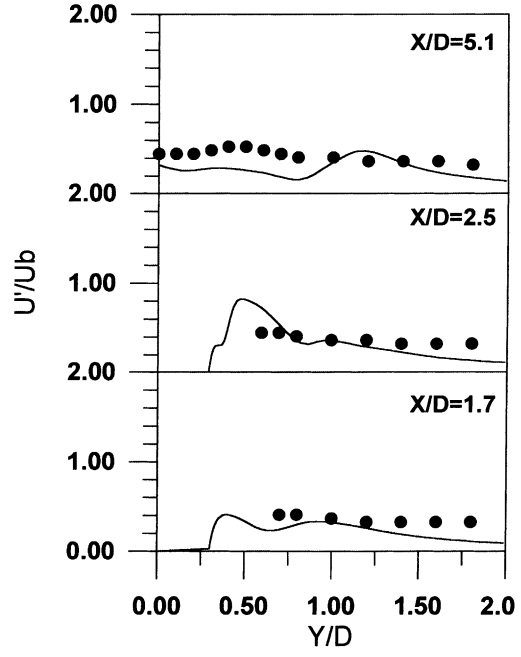

Fig. 3. Comparison between measurements (•) and predictions (lines) for axial velocity fluctuations.

3.3. Numerical computations of two-phase turbulent flow in full-scale in-line arrangements

From here on the calculations of the full-scale geometries will be presented. For all three cases, the flow velocity

upstream of the bundle was uniform at 10 m/s and the temperature 1000 K. Gravity is in the $(-x)$ direction and the mass loading of the particulate phase was 1% (0.0096 kg/s). The Reynolds number is $Re_{dg} = 4300$, which is in the same range as the Reynolds number studied in the laboratory-scale configuration. The rows are numbered in the x direction so that all configurations have a total of six rows. Periodic boundary conditions have been applied on the upper and lower boundary of the domain for all cases.

The flow was calculated using a time step of 1.2E − 4 s and was considered to have stabilized by monitoring flow variables at specific positions until their mean values were stabilized. After this time, 360 000 particles were injected over a total of 150 time steps, which corresponds to roughly one period of the main vortex shedding motion, and then they were tracked until they left the computational domain. The particle distribution and properties were chosen to correspond to those sampled and observed during the operation of the utility boilers of the PPC of Greece. The diameter range of the particles was 23–850 μm and they were distributed into the following mass distribution: of 23, 68 μm: 36.7%; 118, 173 μm: 27.2%; 250, 350 μm: 23.3%; 550, 850 μm: 12.8%. A characteristic particle density of 2300 kg/m^3 was used with particle material properties (Poisson ratio, Young's modulus, etc.) taken to be those of Al_2O_3. Results concerning the particulate phase are averaged over the 150 time steps of their injection thus giving the mean values over this time period.

3.3.1. In-line arrangement with circular tubes

The computations presented herein have been made for a grid consisting of 91 405 (505 × 181) cells. Fig. 4 shows the mass deposition rate (% of the mass injection rate) on each row as a function of each particle diameter. Most of the deposited mass results from the smallest particle diameters. For the first two rows there is also a small contribution from the largest diameters as well. Particle positions are also shown for the smallest and largest particle diameters at two time instants each. The smaller particles follow the flow while the largest particles impact onto the tubes and are deflected onto neighboring tubes where they enter between tube rows.

It is interesting to note that the jet flapping (calculated shedding frequency 57 Hz, Strouhal number based on gap velocity ~0.157) behind the cylinders acts as a mechanism that sweeps the particles into the inter-row areas of the tube bundle. This mechanism of particle transport to the cylinder surfaces is highly dependent on the particle Stokes numbers $Stk = \rho_p d_p^2 U_b / 18 \mu D$. This was also found numerically and experimentally by Tang et al. (1992) who observed that particles of $Stk \lesssim 1$ will gather in very thin regions along the edges of the vortex structures developing in the plane wakes of a bluff body or a mixing layer. The phenomenon was termed "particle focusing" and is attributed to the sweeping of the particles into the high-speed boundaries of the large-scale flow structures and the stretching of the particles along them. Particles with $Stk \ll 1$ will be dispersed along the boundaries and concen-

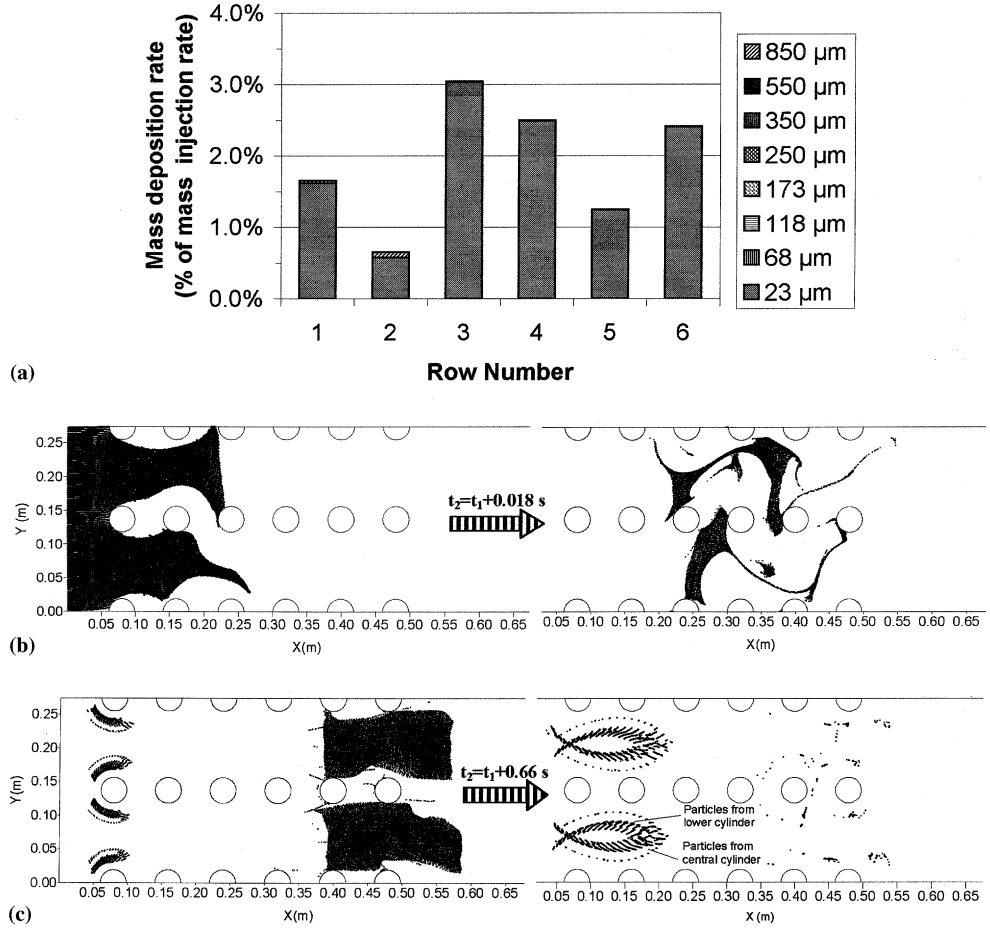

Fig. 4. (a) Deposition rate on tube bundle rows as per each particle diameter. Particle positions at different time instants: (b) 23 μm at $t_1 = 0.018$ s and $t_2 = 0.036$ s; (c) 850 μm, at $t_1 = 0.054$ s and $t_2 = 0.12$ s. Time is measured from the beginning of the particle injection period which lasts $150\Delta t = 0.018$ s.

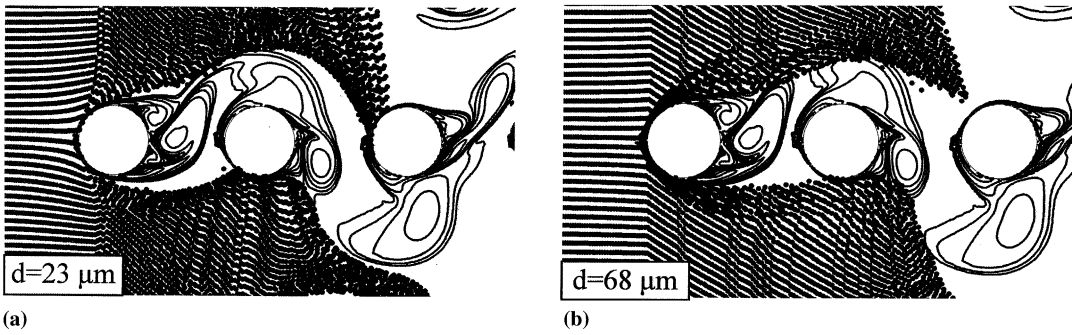

Fig. 5. Particle positions superimposed on iso-vorticity contours at time instant $t = 0.018$ s after beginning of particle injection for (a) 23 μm and (b) 68 μm diameter particles. Close-up view around the first three cylinder rows of the in-line bundle arrangement.

trated inside the vortex structures as well. Larger Stokes number particles will either be thrown out of the vortex due to centrifugal forces or not be affected by it at all and follow the main flow. In the calculation presented here, the effect of the flow's large-scale structures on the particle motion is illustrated in Fig. 5 where the 23 and 68 μm particle positions at time $t = 0.018$ s after the beginning of their injection are superimposed on the flow iso-vorticity contours at the same time instant. These two particle sizes have $Stk(23\ \mu m) = 0.42$, $Stk(68\ \mu m) = 3.67$ and it is evident in the figure that the smaller particles are significantly influenced by the shape of the vortices and are pulled in towards the inter-row regions. In Fig. 5(a) it can be clearly seen that the shape of the vortex leaving the first cylinder is what determines the impact of a series of particles onto the front of the third cylinder. At a later time instant (Fig. 4(b)), the particles have formed the thin lines along the vortex edges as mentioned by Tang et al. (1992) although there is some dispersion partly because the particles' Stokes number is slightly smaller than the critical $Stk = 1$ and partly because of the interaction of the large-scale structures from all of the cylinder rows. This mechanism is not as pronounced for the 68 μm particles (Fig. 5(b)), which tend to pass through the vortex boundaries, while the 850 μm particles (Fig. 4(c)), having $Stk(850) = 573$, are hardly affected by the flow pattern at all.

In order to get further insight into the deposition process, the term Q_i of Eq. (5) (i.e., the kinetic energy of the particle at impact) is examined for the central cylinders (i.e., cylinders with their centers at $y = 0$). This term is normalized with the kinetic energy of a particle with diameter 23 μm moving with the entrance velocity (10 m/s). For brevity of presentation, results are presented for small particles (23 μm), medium sized particles (118 μm) and big particles (850 μm) that impact on the central cylinder of the first and third rows. The variation of the normalized energy for each particle impact along the circumference is presented in Fig. 6. Different symbols are used for particles depending on whether they stick or bounce back. High-energy particles hit the cylinder of the first row on the front stagnation point (in Eq. (5) the particle velocity normal to the cylinder surface is used for the calculation of Q_i). Particles with diameter 23 μm hit part of the frontal area of the first cylinder (45° above and below the front stagnation point) and stick at the point of impact. Note that due to deceleration of the streamwise velocity in front of the first cylinder, the normalized energy of the particles hitting the front stagnation point is less than 1 (around 0.2, which corresponds to velocity at the impact around 45% of the entrance velocity). Bigger particles (118 and 850 μm) are not deflected by the flow field and hit the whole frontal area, i.e., 90° above and below the front stagnation point. Their kinetic energy at the point of impact is 3–5 orders of magnitude larger than the energy of the

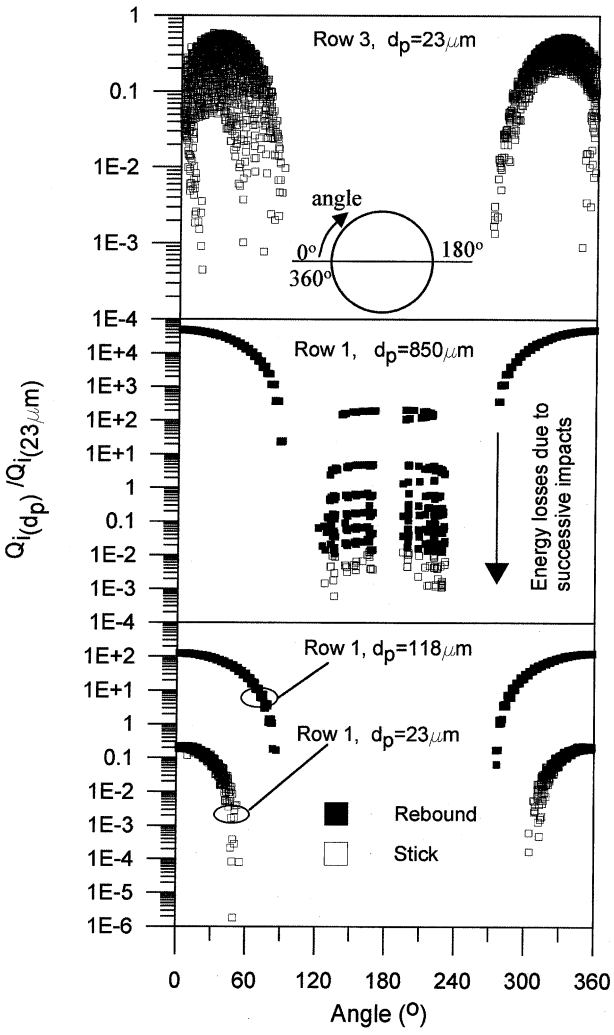

Fig. 6. Normalized kinetic energy distribution along the periphery at the point of impact (Q_i) for different particle diameters at different positions in the in-line array.

23 μm particles and higher than the energy due to attractive forces between particle and surface and thus they rebound. A snapshot of the 850 μm particle positions after rebound is shown in Fig. 4(c). Note that, due to high impact energy, the rebound velocity (Eq. (5)) is high enough so that the big particles from the upper and lower cylinders approach the central

cylinders as shown in Fig. 4(c). They hit the front part of the central cylinders and rebound again finally reaching the back of the upstream cylinders. The implication is that big particles (850 μm) also impact in the area close to the back stagnation point of the central cylinder of the first row (Fig. 6). After each impact the particles lose energy and eventually the energy due to attractive forces becomes dominant and the particles stick in the area around the back stagnation point. This can be seen in Fig. 6 from the gradually decreasing impact energy at 120–240° before the final sticking of the particles. Finally, in Fig. 6, the energy of small particles hitting the third row is shown. The maximum Q_i is at 30–45° above and below the front stagnation point and it is higher than the corresponding maximum value for the first cylinder. This behavior is best understood by looking at Fig. 5(a). The vortex shed from the upper part of the first cylinder traps and accelerates the particles so that they hit the front part of the third cylinder in the area 30–45° away from the front stagnation point. The cycle is completed when a new vortex is shed from the lower part of the cylinder. Note that this vortex shedding process effectively keeps the cylinder on the second row relatively clean and that is why the deposited rate on that cylinder is the smallest (Fig. 4(a)).

From the analysis presented above it becomes clear that the deposition mechanism is characterized by the complex interaction of large-scale vortices and the rebound characteristics of particles. This provides some explanation as to the low deposition rates of the intermediate particle sizes. They are not easily carried away by the vortex structures and also have enough impact energy to rebound but not enough to reach the neighboring tubes as do the 850 μm particles. It is stressed that in a steady-state calculation this mechanism cannot be reproduced.

Having examined in detail the particle–flow interaction for the in-line tube bundle and keeping in mind the impact and deposition mechanisms that were observed, the asymmetric arrangement with circular tubes and the in-line one with elliptic tubes is examined next.

3.3.2. Asymmetric arrangement tube bundle with circular tubes

The computations presented herein have been made for a grid consisting of 168 744 (632 × 267) cells. Fig. 7(a) shows the mass deposition rate (% of the mass injection rate) on each row as a function of each particle diameter. Almost all of the deposit results from the smallest particle diameters. Particle positions are also shown for the smallest and largest particle diameters (Figs. 7(b) and (c)). The smaller particles follow the flow and are swept into the tube bundle by the flapping of the flow behind the cylinder rows (shedding frequency 75 Hz, Strouhal number ~0.2). The increased deposition rate of the second row (Fig. 7(a)) is attributed, not only to its displacement, but also to the increased particle concentration reaching it because of the smaller particles following the boundary layer off of the first row cylinder and impacting onto the second (Fig. 7(b)). The largest particles impact onto the cylinders and are deflected onto neighboring tubes.

The effect of the large-scale vortices on Q_i is shown in Fig. 8. For the central cylinder of row one, the results are almost identical to that of the in-line arrangement, as expected.

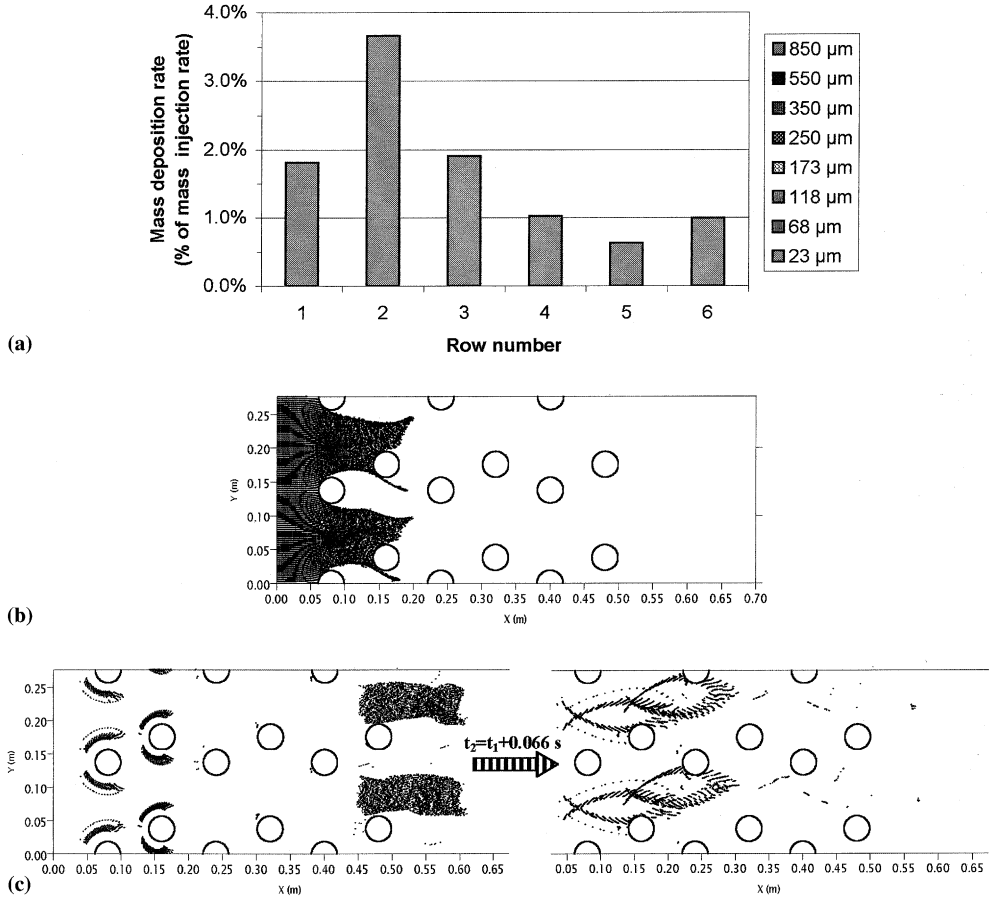

Fig. 7. (a) Deposition rate on tube bundle rows as per each particle diameter. Particle positions at different time instants: (b) 23 μm at $t = 0.0135$ s; (c) 850 μm at $t_1 = 0.054$ s and $t_2 = 0.12$ s. Time is measured from the beginning of the particle injection period which lasts $150\Delta t = 0.0135$ s.

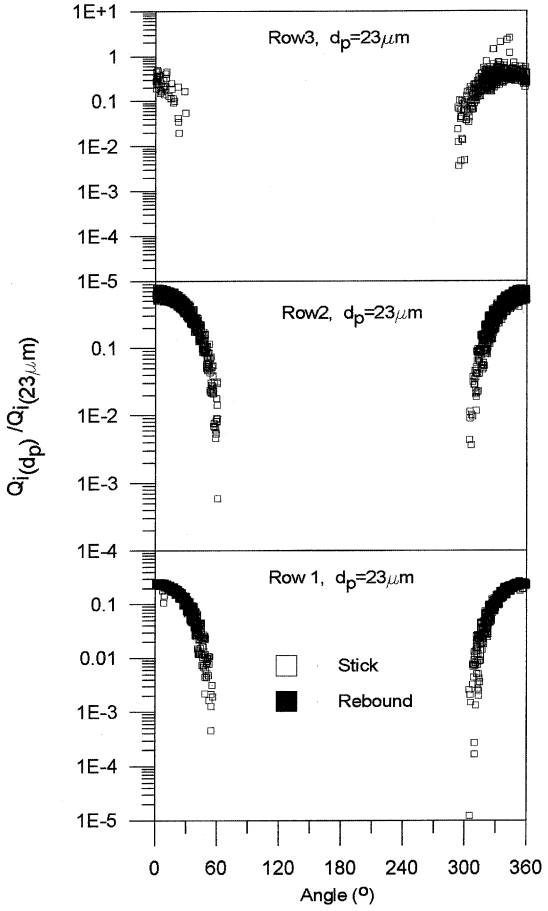

Fig. 8. Normalized kinetic energy distribution along the periphery at the point of impact (Q_i) for the asymmetric array. 23 μm particles at the first, second and third rows of the array.

However, differences are noticed for the central cylinders of the second and third row. For the second row, the kinetic energy of the particles at the point of impact in the area close to the front stagnation point is almost 4–5 times higher that the corresponding energy for the first cylinder. This is attributed to the sweeping effect of the vortex shed from the upper part of the first cylinder, as clearly shown in Fig. 7(b). Thus, in this arrangement the effect of the first cylinder is quite the opposite of that in the in-line arrangement. For this reason, the particle deposition rate is highest in the cylinders of the second row (Fig. 7(a)). The effect of asymmetry is clearly shown in Fig. 8 where the kinetic energy at impact is still high on row three but particles tend to hit the cylinder in the area below the front stagnation point. The deposition rate for the rest of the rows is dependent on the interaction between the particles and the complex vortex shedding patterns present.

Finally, the behavior of large particles (850 μm) is similar to that of the in-line arrangement since they are not affected by the large-scale motion as shown in Fig. 7(c). Since the cylinders are displaced, large particles do not deposit at the rear part of the tubes as in the in-line arrangement.

3.3.3. In-line arrangement tube bundle with elliptic-shaped tubes

The computations presented herein have been made for a grid consisting of 91 405 (505 × 181) cells. For the given tube bundle and operating conditions the frequency of the maximum amplitude of velocity fluctuation behind the first cylinder was calculated to be 40.7 Hz, which corresponds to a Strouhal number of 0.127 based on the gap velocity ($1.22U_b$). The amplitude of this fluctuation is much smaller (about 1/5) than that of the base case, indicating weaker jet flapping and vortex shedding. Fig. 9(a) shows the mass deposition rate on each row as a function of each particle diameter. Again, most of the deposit results from the smallest particle diameters. Particle trajectories are also shown for the smallest and largest particle diameter (Figs. 9(b) and (c)). The effect of the streamlined shape of the tubes and the weak flapping from the first row cylinder is evident in the minimal deposition rate to the second and third row. This underlines the importance of the flapping mechanism in bringing particles into the inter-row areas. The overall deposition rate is smaller than in the base case and this was the desired feature. As will be shown in a following section, the elliptic-shaped tubes also contribute to a smaller pressure drop along the tube bundle.

3.3.4. Comparison of the behavior of the three different arrangements that were studied

An evaluation of the fouling behavior of the three tube bundle configurations that were studied will be presented here. The in-line tube bundle with circular-shaped tubes will be considered as a base case and will be compared with the deposition rates for the asymmetric arrangement tube bundle and the in-line tube bundle with elliptic-shaped tubes. As observed in Figs. 4, 7 and 9, the overwhelming majority of the deposit is from the smallest diameter particles (23 μm) with the contribution of the largest diameters (850 μm) being noticeable for the in-line tube bundle with circular tubes. In Fig. 10 the deposition rates for the three tube bundle configurations are presented in relation to the deposition rate of the in-line arrangement with the contribution to each tube bundle row being the second parameter. The predicted deposition rates of the asymmetric arrangement and the in-line tube bundle with elliptic-shaped tubes are 12% and 73% lower, respectively, than that of the base case. For the in-line tube bundle and the asymmetric arrangement, the contribution to the first cylinder is almost identical while the asymmetric tube bundle shows a pronounced increase in the deposition rate of the second row. This is the displaced row that is "protected" by the first in the in-line arrangements. For the in-line arrangement with elliptic tubes, the second row shows minimal deposits. The first row of the tube bundle with elliptic-shaped tubes also shows the lowest deposition rate of the three configurations that were studied.

Note that the above results on fouling deposition rate correspond to tubes that are initially clean. However, the deposited mass will alter the tube shape and this will subsequently alter the flow field and the particle deposition rate at later times. This has been studied in Bouris and Bergeles (1997) where both the heat transfer through the deposit and the effect on subsequent deposit was calculated. Comparison with experimentally observed deposition rates and heat transfer is also made in Bouris and Bergeles (1997) and favorable agreement validates the numerical calculations. The arrangement that will be faster affected by the deposit buildup is the asymmetric one, especially the second row where the predicted particle deposition rate is the largest. Thus it is possible that the first and second cylinders in the middle row may be bridged by material deposited on the latter cylinder. This will change the flow field in the other parts of the tube bundle as well. In order to account for this effect, a time-dependent particle deposition model must be developed and the flow field must be recalculated when there is tube shape alteration due to the deposited material.

When comparing the average pressure drop (as a percentage of the pressure drop for the in-line tube bundle) for each arrangement, it is found that the in-line arrangement with

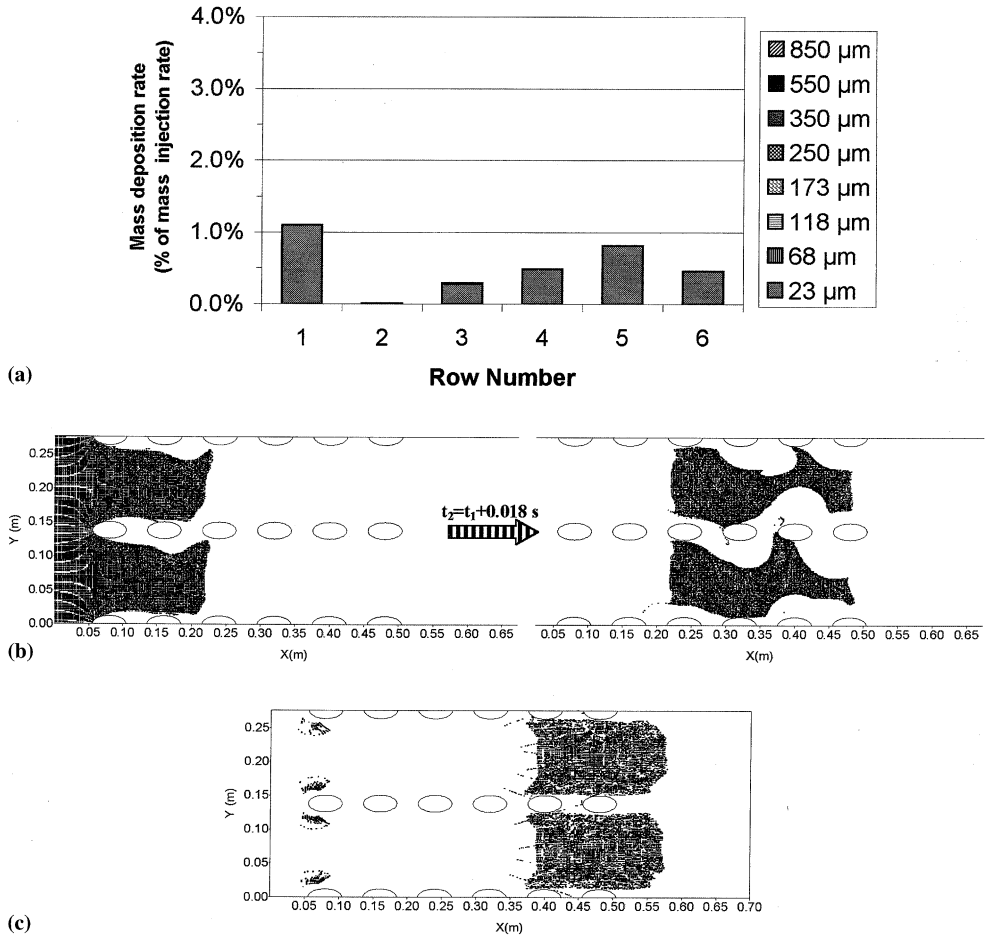

Fig. 9. (a) Deposition rate on tube bundle rows as per each particle diameter. Particle positions at different time instants: (b) 23 μm at $t_1 = 0.018$ s and $t_2 = 0.036$ s; (c) 850 μm, at $t = 0.054$ s. Time is measured from the beginning of the particle injection period which lasts $150\Delta t = 0.018$ s.

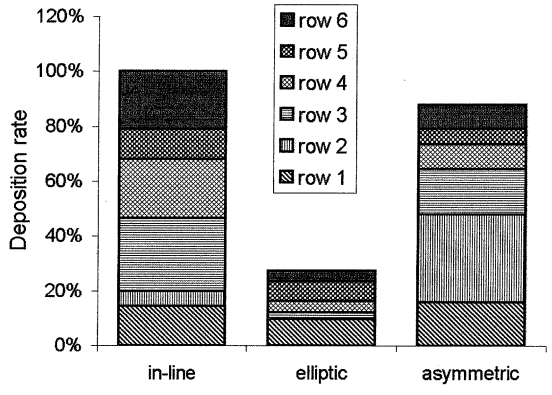

Fig. 10. Deposition rate on tube bundle arrangements as per each row (1 is the upstream row, 6 is the last row of the tube bundle). Non-dimensionalized by total deposition rate for in-line tube bundle.

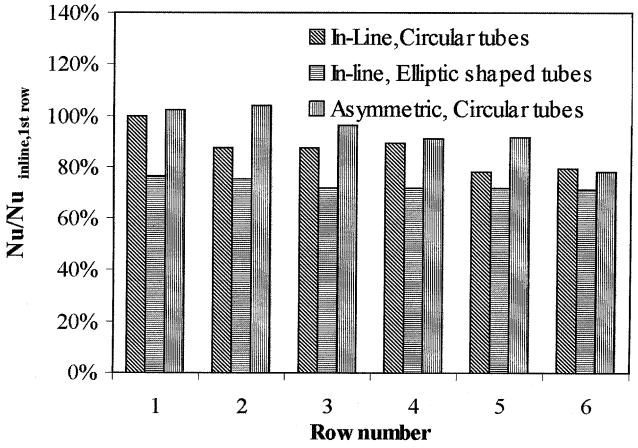

Fig. 11. *Nu* number for each row for the three arrangements examined. Non-dimensionalized by the *Nu* number for the first row cylinder of the in-line bundle arrangement.

elliptic-shaped tubes exhibits an 81% reduction compared to that of the base case in-line tube bundle. This is expected due to the streamlined shape of the elliptic tubes. On the other hand, the asymmetric tube bundle shows an 18% increase in pressure drop compared to the standard in-line configuration, which can be attributed to the displaced rows that act as additional obstacles to the flow.

In Fig. 11 the *Nu* number for each row is presented for all arrangements. Results are presented as a percentage of the calculated Nusselt number of the first row cylinder in the in-line base case. For comparison purposes, we note that according to Incropera and DeWitt (1996), for an in-line tube

bundle at the operating conditions being studied, the mean Nusselt number for a six-row tube bundle should be around $Nu = 43.8$ while the calculated Nusselt number for the arrangement under study is about $Nu = 33.6$. This amounts to a difference of 22% which could be attributed to differences in the turbulence levels upstream of the bundle, the constant temperature boundary condition that was used, etc. For the purposes of comparing the arrangements though, this level of accuracy should not affect the conclusions that are drawn.

The asymmetric arrangement results in a slight overall increase in heat transfer rates. Note that for all rows the heat transfer rate is lowest for the in-line arrangement with elliptic-shaped tubes. For the whole bundle the reduction is around 16% as compared to the base case. The reduction is attributed to the streamlined shape of the tubes and the reduction in production of turbulence. Considering also the level of accuracy of the predictions, it would be safe to say that this drawback could be overcome by placing more tube rows in the same area since the reduction in deposition rate and pressure drop seems to permit it.

The in-line tube bundle with elliptic-shaped tubes shows a marked decrease in fouling potential combined with a reduction in pressure drop along the bundle. Taking this into consideration, a closer spacing of the tubes could be implemented. This would lead to more tube rows and therefore a larger heat transfer area while preserving low values of deposition rate and pressure drop.

4. Conclusions

A previously developed numerical methodology was used to calculate the fouling behavior of three different tube bundle configurations. The methodology is a time-dependent calculation based on volume averaging of the Navier–Stokes equations and subgrid-scale modeling of the small-scale turbulence. The particulate phase is treated in a Lagrangian manner and an energy balance is used to determine the particle adhesion or rebound from a solid surface to which it impacts. The methodology is first validated for the flow under examination by simulating the turbulent cross-flow through a laboratory-scale in-line tube bundle and acceptable agreement with experimental measurements is found. Following this, the method is applied to study the fouling behavior of three different tube bundle configurations: a standard in-line tube bundle with circular tubes, an in-line tube bundle with elliptic-shaped tubes and an asymmetric arrangement tube bundle with circular tubes. It is noted that the results refer to the initial deposition rates. As the deposit builds up, the tube shape will alter and deposit removal will also take place. These two mechanisms should be taken into account in order to obtain even more reliable insight into the phenomenon and they are the subject of ongoing research by the authors.

Through the time-dependent calculation, the effect of the vortex shedding in the tube bundle is found to play an important role in particle deposition in the inner tube bundle rows. Smaller particles are carried into the inter-row areas by the vortex flapping motion and thus deposition is facilitated. This mechanism is highly dependent on the particle Stokes numbers and the vortex patterns in the tube bundle and it could not be calculated with a steady-state calculation.

Particle deposition rate in the in-line tube bundle with circular tubes is calculated to be the highest of the three configurations studied here. The asymmetric arrangement inhibits vortex shedding intensity and deposition rates to the downstream rows is found to be reduced. However, this effect is countered by the displaced tubes, which act as obstacles and facilitate deposition. The overall deposition rate to the asymmetric tube bundle is found to be reduced by about 12%. For the in-line arrangement with elliptic-shaped tubes, vortex shedding is reduced due to the tube shape while retaining the in-line arrangement. The reduced frontal area of the tubes and the more streamlined shape also reduce the deposition rates. Overall, the use of elliptic-shaped tubes leads to a 73% reduction in deposition rate. Furthermore, the elliptic-shaped tubes reduce the pressure drop along the bundle by 81% while the asymmetric arrangement increases it by 18%.

The heat transfer efficiency of the elliptic-shaped tubes is reduced due to the streamlined shape and the reduction in production of turbulence but this could be overcome by placing more tube rows in the same area. This is practically and economically feasible due to the low pressure drop and deposition rates.

Concluding, it seems that the use of elliptic-shaped tubes gives promising indication to allow increase of the heat transfer surfaces while preserving low values of pressure drop and fouling rates.

Acknowledgements

The research was funded in part by the European Commission in the framework of the JOULE III program, contract No. JOUE3-CT97-0064.

References

Barsamian, H., Hassan, Y., 1997. Large eddy simulation of turbulent crossflow in tube bundles. Nucl. Eng. Des. 172, 103–122.

Bitter, J.G.A., 1963. A study of erosion phenomena (Part II). Wear 6, 169–190.

Bouris, D., Bergeles, G., 1996. Particle–surface interactions in heat exchanger fouling. J. Fluids Eng. 118, 574–581.

Bouris, D., Bergeles, G., 1997. Numerical calculation of the effect of deposit formation on heat exchanger efficiency. Int. J. Heat Mass Transfer 40 (17), 4073–4084.

Bouris, D., Bergeles, G., 1999. Two-dimensional time dependent simulation of the subcritical flow in a staggered tube bundle using a subgrid scale model. Int. J. Heat Fluid Flow 20, 105–114.

Clift, R., Grace, J., Weber, M., 1978. Bubbles, Drops and Particles. Academic Press, New York.

Couch, G. 1994. Understanding slagging and fouling in pf combustion. IEACR/72, IEA Coal Research, London.

Fowkes, F., 1964. Attractive forces at interfaces. Ind. Eng. Chem. 56 (12), 40–52.

Incropera, F.P., DeWitt, D.P., 1996. Fundamentals of Heat and Mass Transfer, fourth ed.. Wiley, New York.

Konstantinidis, S., Castiglia, D., Balabani, S., Yianneskis, M., 2000. Velocity and vortex shedding characteristics of an in-line tube bundle in steady and pulsating crossflow. Trans. IChemE Chem. Eng. Res. Des. 78 (A8), 1129–1138.

Lilly, D., 1967. The representation of small scale turbulence in numerical simulation experiments. In: Goldstine, H.H. (Ed.), Proceedings of the IBM Scientific Computing Symposium on Environmental Sciences. IBM Form No. 320-1951, pp. 195–210.

Mouzakis, G., Bergeles, G., 1991. Numerical prediction of turbulent flow over a two dimensional ridge. Int. J. Numer. Meth. Fluids 12, 287–296.

Ota, T., Nishiyama, H., Kominami, J., Sato, K., 1986. Heat transfer from two elliptic cylinders in tandem arrangement. J. Heat Transfer 108, 525–531.

Ota, T., Nishiyama, H., Taoka, Y., 1984. Heat transfer and flow around an elliptic cylinder. Int. J. Heat Mass Transfer 27 (10), 1771–1779.

Papadakis, G., Bergeles, G., 1995. A locally modified second order upwind scheme for convection terms discretisation. Int. J. Numer. Meth. Heat Fluid Flow 5, 49–62.

Patankar, S.V., Spalding, D.B., 1972. A calculation procedure for heat, mass and momentum transfer in three dimensional parabolic flows. Int. J. Heat Mass Transfer 15, 1787.

Reed, J., 1985. Energy losses due to elastic wave propagation during an elastic impact. J. Phys. D 18, 2329–2337.

Rhie, C., Chow, W., 1983. Numerical study of the turbulent flow past an airfoil with trailing edge separation. AIAA J. 21, 1525–1532.

Rollet-Miet, P., Laurence, D., Ferziger, J., 1999. LES and RANS of turbulent flow in tube bundles. Int. J. Heat Fluid Flow 20, 241–254.

Saffman, P., 1965. The lift on a small sphere in a slow shear flow. J. Fluid Mech. 22, 385; Corrigendum 1968, 31, 624.

Schumann, U., 1975. Subgrid scale model for finite difference simulations of turbulent flows in plane channels and annuli. J. Comput. Phys. 18, 376–404.

Smagorinsky, J., 1963. General circulation experiments with the primitive equations. I. The basic experiment. Mon. Weather Rev. 91, 99–164.

Talbot, L., Cheng, R.K., Schefer, R.W., Willis, D.R., 1980. Thermophoresis of particles in a heated boundary layer. J. Fluid Mech. 101 (4), 737–758.

Tang, L., Wen, F., Yang, Y., Crowe, C., Chung, J., Troutt, T., 1992. Self-organising particle dispersion mechanism in a plane wake. Phys. Fluids A 4 (10), 2244–2251.

Wall, S.M., John, W., Goren, S.L., 1988. Application of impact adhesion theory to particle kinetic energy loss measurements. In: Mittal, K.L. (Ed.), Particles on Surfaces 2. Plenum Press, New York.

Wang, Q., Squires, K., 1996. Large eddy simulation of particle deposition in a vertical channel flow. Int. J. Multiphase Flow 22 (4), 667–683.

Wung, T., Niethammer, J., Chen, C. 1986. Measurements of heat–mass transfer and pressure drop for some non-standard arrays of tubes in crossflow. In: Tien, C., Carey, V., Ferrell, J. (Eds.), Heat Transfer 1986, Proceedings of the Eighth International Heat Transfer Conference. Hemisphere, San Fransisco, pp. 1041–1046.